

Turning *gelidium amansii* residue into nitrogen-doped carbon nanofiber aerogel for enhanced multiple energy storage

Daohao Li^a, Yu Wang^a, Yuanyuan Sun^a, Yun Lu^b, Shuai Chen^c, Bingbing Wang^a,
Huawei Zhang^d, Yanzhi Xia^{*a}, Dongjiang Yang^{*a,e}

^aCollaborative Innovation Center for Marine Biomass Fibers, Materials and Textiles of Shandong Province, Institute of Marine Biobased Materials, School of Environmental Science and Engineering, Qingdao University, Qingdao 266071, P. R. China.

^bDepartment of Wood Anatomy and Utilization, Research Institute of Wood Industry, Chinese Academy of Forestry, Beijing 100091, P. R. China.

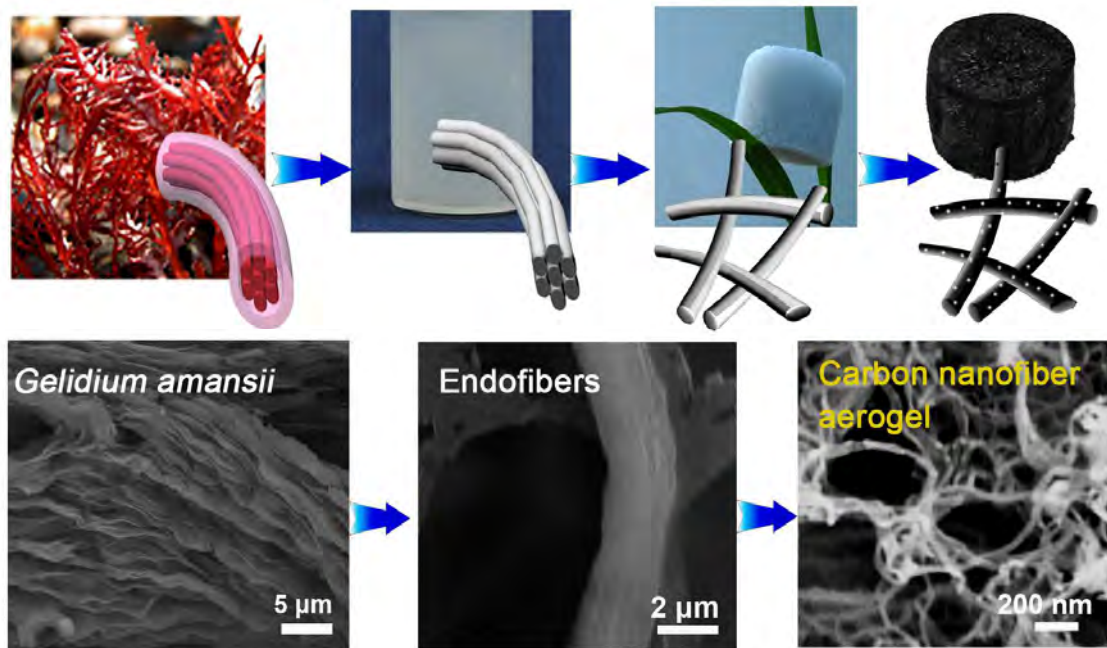
^cState Key Laboratory of Coal Conversion, Institute of Coal Chemistry, Chinese Academy of Science, Taiyuan 030001, P. R. China.

^dCollege of Chemical and Environmental Engineering, Shandong University of Science and Technology, Qingdao 266590, P. R. China.

^eQueensland Micro- and Nanotechnology Centre (QMNC), Griffith University, Nathan, Brisbane, Queensland 4111, Australia.

Corresponding authors: E-mail: d.yang@qdu.edu.cn (D. Yang); xiayz@qdu.edu.cn (Y. Xia)

GRAPHICAL ABSTRACT



ACCEPTED MANUSCRIPT

Abstract

Three-dimensional (3D) carbonaceous aerogels assembled by one-dimensional (1D) carbon nanofibers (CNF) have attracted much attention, because their unique interconnected and hierarchical porous structure can offer a wide range of applications in environmental remediation and energy storage. Herein, the residue of *gelidium amansii* (mainly endofibers, $\sim 1.6 \mu\text{m}$) after extraction of agar were used as precursor to fabricate nanofibrilated cellulose by using facile ultrasonication treatment. The nanofibrilated celluloses are highly engineered nanofibers with average diameter of $\sim 90 \text{ nm}$. Then the 1D cellulose nanofibers could be assembled into 3D nanofiber aerogels after freeze drying. The subsequent pyrolysis in NH_3 and activation could result in the formation of N-doped CNF aerogel (N-PCNFA), where the oxygen-containing groups in cellulose macromolecules converted to H_2O , CO , and CO_2 . The N-PCNFA with hierarchically porous structure, high surface area ($2290 \text{ m}^2 \text{ g}^{-1}$), N-doping, and 3D interconnected channels are beneficial to electrolyte ions and electron transportation. The N-PCNFA displayed high capacity and long-term stability as energy storage material. This work highlights a new strategy in highly efficient utilizing the marine biomass waste for developing low-cost and functional carbon aerogel for multiple energy storage.

Carbon nanomaterials, including carbon nanotube, carbon nanosphere, graphene, and carbon nanofiber (CNF) etc, have been considered as the promising energy storage materials for lithium ion batteries (LIBs) and supercapacitors (SCs), due to their relatively high electronic conductivity, high specific capacity, accessibility, and excellent stability [1-3]. Particularly, one-dimensional (1D) CNF has been extensively explored for energy storage because of its oriented electronic/ionic transport pathway, excellent mechanical property, and high surface to volume ratio [4, 5]. However, the ordinary CNF usually cannot meet the increasing requirement for excellent performance energy storage devices due to its dissatisfactory electrolyte ions and electron transports. Constructing porous structure in CNF with high surface area offer sufficient porous channels and large interface between active sites and electrolyte for promoting the electrolyte ion diffusion, which can achieve the high requirement of energy storage devices [6-9]. Recently, three-dimensional (3D) carbonaceous aerogels assembled by 1D porous CNF have been attracted much attention. The adequate space of hierarchically 3D interconnected CNF-based framework and high length-diameter ratio of 1D CNF could synergistically promote electrolyte ions diffusion and electron transport, further enhancing the energy storage performance.

Generally, the fabrication of such 3D hierarchical porous CNF depends on the pyrolysis of polymer (such as poly(vinyl alcohol), polyacrylonitrile, and polyimide) nanofiber through simple electrospinning synthetics, generating continuous nanofibers with controlled size [10, 11]. The non-renewable polymer precursors and toxic by-products hinder the sustainable applications of such CNF. Thus, low-cost, sustainable, and large-scale production of 3D porous CNF with cheap and renewable precursors is still a vital research demand. Nowadays, many valuable CNF derived from sustainable

biomass have been developed through innovative strategies, which show great potential in energy storage [12-15]. For example, bacterial cellulose is a promising candidate for the fabricating of CNF, opening a green and sustainable biomass-converting method. Lu *et al.* controllably synthesized a series of 3D porous CNF aerogel with different dimeters using earth-abundant bamboo as precursors [12]. With the fast exploration of ocean, the abundant algae resources, mainly including brown, red, and green algae, have been extensively concerned [16-25]. Similar to bamboo, some of abundant seaweed (~ 30,000,000 tons per year) contain high cellulose, making them possible to produce CNF aerogel *via* a sustainable route. For instance, *Gelidium amansii* (GA), one of the most abundant red algae species, mainly is composed of mucilaginous materials and endofibers. After the extraction of agar or carrageenan from polysaccharide complexes of the mucilaginous materials, the remaining solid endofibers are cellulose (8%-11%) [26, 27]. However, the GA residue shows low value for further utilization at present.

Herein, we used such GA residue (mainly endofibers, ~1.6 μm) as precursor to fabricate nanofibrilated cellulose by using facile ultrasonication treatment, since the ultrasonication process could break the weak macromolecular interfibrillar hydrogen bonding and Vander Waals force. The nanofibrilated celluloses are highly engineered nanofibers with average diameter of ~90 nm. Then the 1D cellulose nanofibers could be assembled into 3D nanofiber aerogels after freeze drying. The subsequent pyrolysis in NH_3 and activation could result in the formation of N-doped CNF areogel (N-PCNFA). When used as energy storage material, the important characteristics of N-PCNFA, such as 3D interconnected network, high surface area (2290 $\text{m}^2 \text{g}^{-1}$), porous structure and N-doping, not only increase the contact surface area of active material and electrolyte to

decrease ion diffusion distance, but also enhance the conductivity of electrode material. For instance, as lithium storage material, N-PCNFA exhibits a high specific capacity and good cycling stability (572 mAh g⁻¹ at 1 A g⁻¹ after 600 cycles), and excellent rate performance (220 mAh g⁻¹ at high current density of 10 A g⁻¹). It also displays the excellent capacitive behavior (in a three-electrode system, 320 and 248 F g⁻¹ at 1 and 100 A g⁻¹, respectively) for SCs.

2. Experimental Section

2.1. Materials preparation

The GA was firstly decolorized by NaClO₂ solution to produce bleached GA pulp, and washed with H₂O to pH = 7. Then, the obtained sample was treated with 1 M KOH solution at 85 °C for 2 h, which has a significant and positive effect on solubilizing the agar from the GA. After filtration, the filtered residue was endofiber (mainly cellulose). To fabricate cellulose nanofiber, the typically ultrasound method was used. The residue was put in a beaker with water, and then the pulsed high-intensity (60 KHz, 300 W) ultrasonication was performed with the water/ice bath for 30 min (setting 50 % duty cycle for reducing temperature variation). The nanofibrillated cellulose was obtained, and the cellulose nanofiber/water dispersion was frozen to -70 °C. The freeze-drying was used to dry it to get the cellulose nanofiber aerogel. Then, the cellulose nanofiber aerogel was pyrolyzed at 700 °C for 1 h under the ammonia or nitrogen atmosphere (heating rate: 2 °C min⁻¹) to fabricate the N-doped carbon nanofiber aerogel (N-CNFA) and carbon nanofiber aerogel (CNFA), respectively. The N-CNFA and CNFA were activated by KOH at 800 °C for 1 h (weight ratio of KOH/samples = 4/1) under nitrogen atmosphere and then washed with 1 M HCl and deionized water until pH=7 to obtain the N-PCNFA and PCNFA, respectively.

2.2. Characterization.

Scanning electron microscopy (SEM) images were obtained using a JSM-7001F instrument. Transmission electron microscopy images (TEM) were obtained using a JEM-2100F electron microscope with an accelerating voltage of 200 kV. Coupled thermogravimetric analysis and mass spectrum were obtained using Evolution 16/18 and OMNI star instruments. The crystal structures of samples were characterized by X-ray diffraction (XRD, DX2700, China). Raman spectroscopy (Renishaw 1000NR) was performed at room temperature on a Renishaw 1000 Raman spectrometer using an Ar ion laser at 514.5 nm excitation line. The specific surface area was calculated by the Brunauer-Emmett-Teller (BET) method from data in a relative pressure (P/P_0) range between 0.001 and 0.25 and pore size distribution plots were derived from the adsorption branch of the isotherms based on the BJH model. The chemical composition was investigated by X-ray photoelectron spectroscopy (XPS) using an ESCALab250 electron spectrometer (Thermo Scientific Corporation) with monochromatic 150 W Al $K\alpha$ radiation.

2.3. Electrochemical measurements.

The obtain samples were mixed with poly (vinylidene fluoride) (PVDF) and acetylene black at a weight ratio of 8:1:1 using the N-methyl-2-pyrrolidone (NMP) as solution. Then, the resultant slurry was uniformly pasted on Cu foil and dried in a vacuum oven at 120 °C for 10 h. The electrolyte was the solution of 1 M LiPF_6 in ethylene carbonate (EC)/dimethyl carbonate (DMC)/diethyl carbonate (DEC) (1:1:1, in wt%). CR2016-type coin cells were assembled in a glove box using Li metal foil as both the counter and reference electrodes. Cyclic voltammetry (CV) was performed using on a CHI 760 E electrochemical workstation (CH Instruments, Inc.). The

galvanostatic charge/discharge (GCD) tests were conducted using a cell testing instrument (LAND CT2001A).

The samples were tested on three-electrode system and two-electrode system with 6 M KOH as the electrolyte for SCs. In a three-electrode measurement system, Pt wire, Ag/AgCl, and Ni foam were used as the counter, reference electrodes, and current collector, respectively. For the two-electrode cells, the electrodes were prepared by mixing 85 wt% active materials, 10 wt% carbon black, and 5 wt% poly-(vinylidene fluoride). The loading density of the electrode is about 2 mg cm⁻². The CV, GCD, and electrochemical impedance spectrum (EIS) test were performed using the CHI 760E electrochemical workstation. For quantitative considerations, the specific capacitances of the samples were calculated from the GCD values tested on three-electrode system according to the formula (1) and two-electrode system according to the formula (2):

$$C = \frac{I \times \Delta t}{m \times \Delta V} \quad (1)$$

$$C = \frac{2I \times \Delta t}{m \times \Delta V} \quad (2)$$

where C (F g⁻¹) is the specific capacitance, I (A) is the discharge current, Δt (s) is the discharge time, m (g) is the total mass of the one electrode material, and ΔV (V) is the potential window.

3. Results and discussion

3.1 Characterization of N-PCNFA

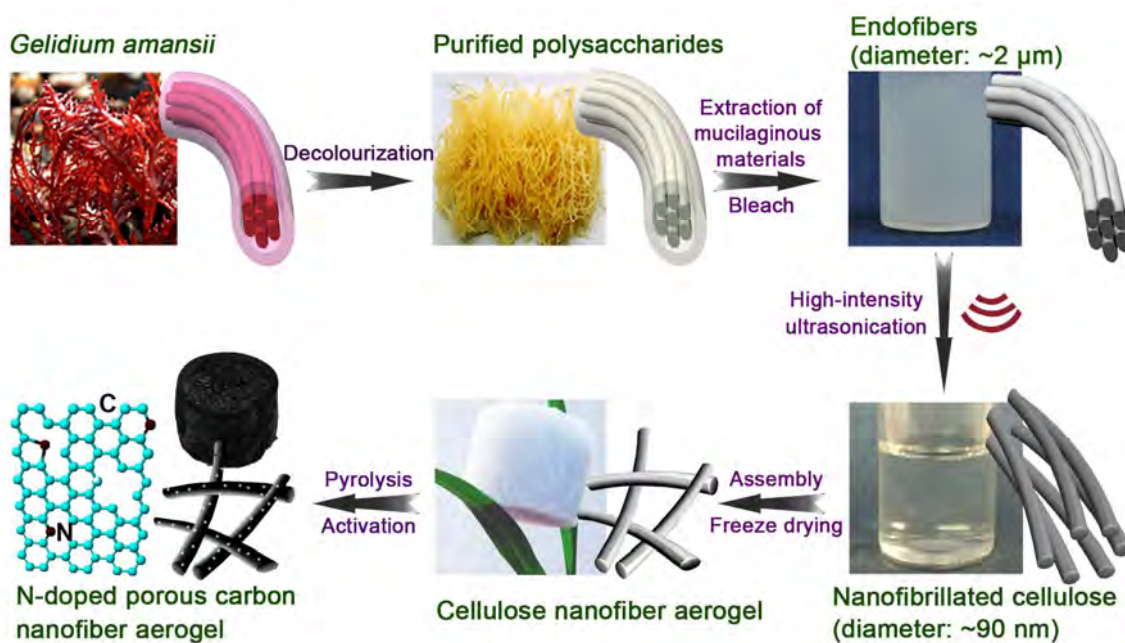


Fig. 1. Schematic illustration on the synthesis process of N-PCNFA.

The preparation process of N-PCNFA is illustrated in Fig. 1. The GA were collected from Qingdao coastal waters. In the first step, the GA was chemical purified like decolorization and demineralization to remove impurities like mud, dirt, surface attached substances, and the red colour to obtain purified GA. Then, the wetted bleached endofiber with average diameter of $\sim 1.6 \mu\text{m}$ can be obtained from extracting the agar from GA through the processes of bleaching, dissolution, and filtration. In this process, agar, sugar, and starch were removed, and the algal cellulose were retained. Given that ultrasonic cavitation can break the macromolecular interfibrillar hydrogen bonding and the Vander Waals force [28, 29], ultrasonication treatment could gradually disassemble the micro-scale endofibers into nanofibers. The cellulose nanofibers with average diameter of $\sim 90 \text{ nm}$ were obtained after ultrasonication treatment (60 KHz, 300 W) of 30 min during which the endofiber/water suspension converts to clear solution. Then after *tert*-butyl alcohol freeze-drying, the 1D cellulose nanofiber building blocks assembled into 3D aerogel. To fabricate highly porous N-doped carbon nanofiber

aerogel (N-PCNFA), the cellulose nanofiber aerogel was pyrolyzed (700 °C) in the presence of NH₃ atmosphere and then was activated by using potassium hydroxide activation (800 °C) for 1 h.

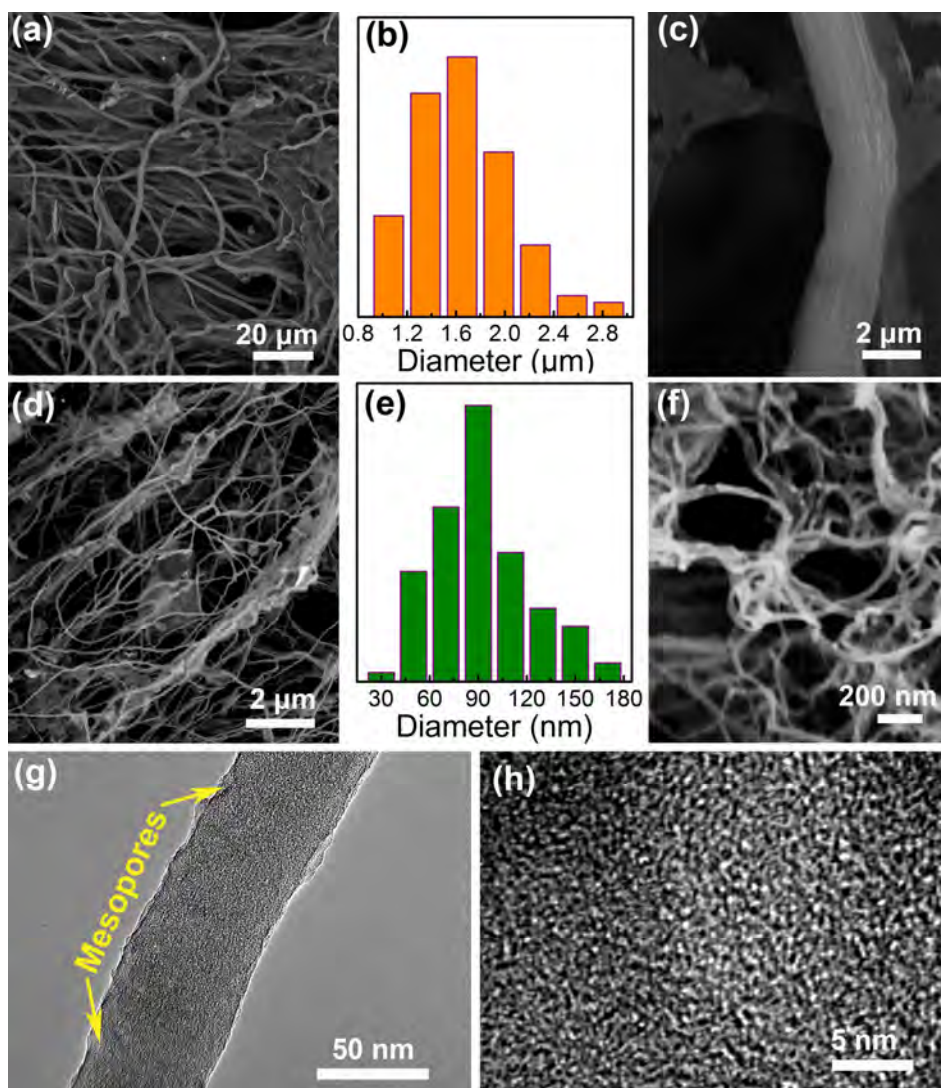


Fig. 2. SEM images of (a, c) the fibrous cellulose, (d) the cellulose nanofiber aerogel, and (f) N-PCNFA. The diameter distributions of (b) the fibrous cellulose, and (e) the cellulose nanofiber aerogel. (g) TEM and (h) HRTEM images of N-PCNFA.

The morphologies of the prepared cellulose endofiber, cellulose nanofiber aerogel, and N-PCNFA were determined by scanning electron microscopy

(SEM). The crumpled GA contains bundled and stacked fibrous cellulose (Fig. S1). In the agar extraction process, the cytoderm of GA is destroyed by chemicals and the GA residue is fibrous cellulose with obvious fibrous morphology (Fig. 2a). The average diameter of the endofibers is $\sim 1.6 \mu\text{m}$ (Fig. 2b). Such endofibers also exhibit crumpled surface (Fig. 2c). Fig. 2d shows the morphology of cellulose nanofiber aerogel after ultrasonication treatment, producing slender cellulose nanofibers with average diameter of $\sim 90 \text{ nm}$ (Fig. 2e). After pyrolysis in NH_3 atmosphere and KOH activation, the N-PCNFA sample was obtained. X-ray diffraction (XRD) pattern of N-PCNFA shows broad diffraction peaks located at about 25° , which corresponds to amorphous carbon structure (Fig. S2). Its aerogel morphology inherits from the cellulose nanofiber aerogel (Fig. 2f). However, the average diameter of the carbon nanofibers reduces to $\sim 50 \text{ nm}$, only half of that of the cellulose nanofibers due to the decomposition of cellulose. The transmission electron microscopy (TEM) was used to characterize microstructure of the N-PCNFA. As shown in Fig. 2g, the small-sized mesopores ($< 10 \text{ nm}$) are observed in a single carbon nanofiber. This mesoporous structure can offer an avail the electrolyte storage to shorten the electrolyte ions diffusion distance, enhancing the electrochemical performance [30]. The high resolution TEM (HRTEM) image illustrates that the N-PCNFA shows amorphous carbon structure (Fig. 2h).

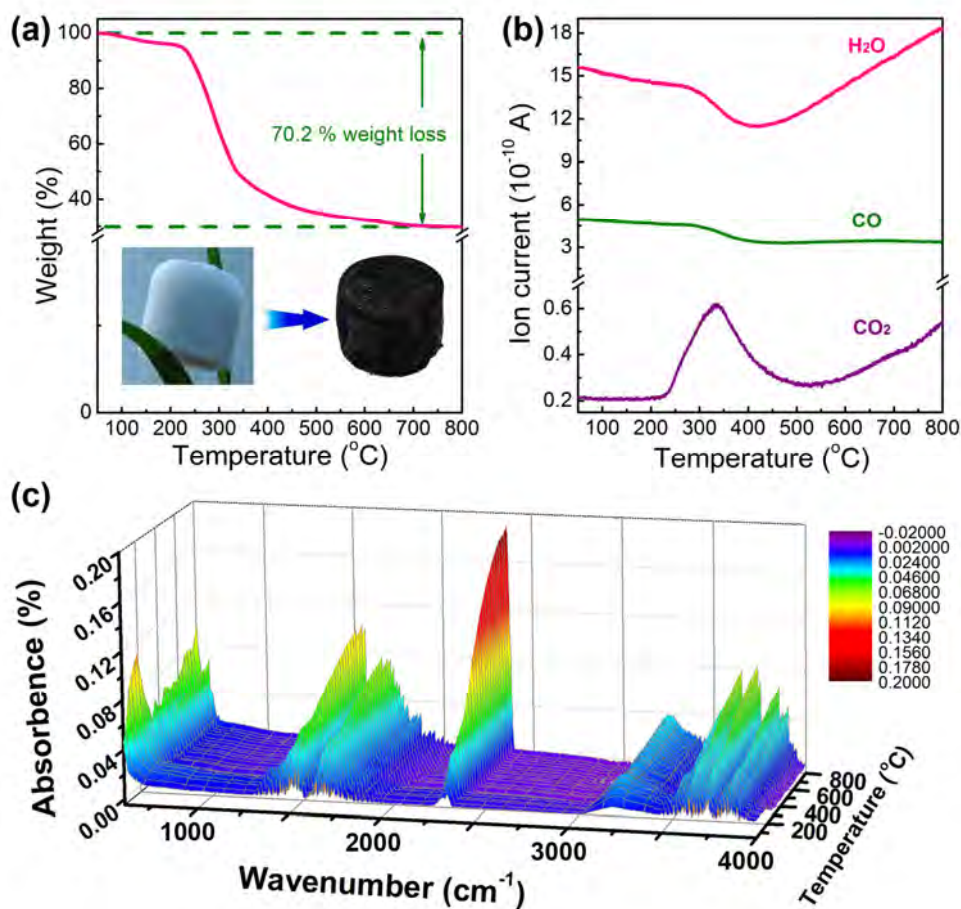


Fig. 3. (a) TGA curve of cellulose nanofiber aerogel in N₂ atmosphere ((heating rate of 5 °C min⁻¹). (b) The analysis of the outlet gases from the decomposition of cellulose nanofiber aerogel TG-MS: H₂O (pink), CO (olive), and CO₂ (purple). (c) 3D spectra of TG-FTIR of cellulose nanofiber aerogel.

To reveal decomposition process of the cellulose nanofiber aerogel, coupled thermogravimetric and mass spectrum (TG-MS) was carried out. The TG curve of the cellulose nanofiber aerogel presents one distinct weight losses at a temperature range of 230-380 °C (Fig. 3a). Fig. 3b shows the corresponding mass spectra for TG curve, which demonstrates the evolved gases are H₂O (m/z: 18), CO (m/z: 28), and CO₂ (m/z: 44). At the all the decomposition process, a mass of H₂O, CO, and CO₂ are evolved from the cellulose macromolecules. A

obvious peak is observed at 340 °C from the purple curve (CO₂), which is ascribed to the fast decomposition stage at around 230-470 °C (Fig. 3a), corresponding to the TG curve. Thus, the whole thermal decomposition process of the cellulose nanofiber aerogel is the oxygen-containing groups (such as -C-O-C-, and -OH) in cellulose macromolecular converted to H₂O, CO, and CO₂. The product of the pyrolysis process is the CNFA with 29.8 wt% retention. TG-Fourier transform infrared spectroscopy (TG-FTIR) spectra in the thermal decomposition process of cellulose nanofiber aerogel further gave the evidence for the gas components evolved. As shown in Fig. 3c, the peaks located at 3851-3253 cm⁻¹ and 2360 cm⁻¹ in all the spectra indicate the release of H₂O vapour and CO₂ in the whole pyrolysis process. The two peaks positioned at 1682 and 1541 cm⁻¹ are ascribed to the stretching vibration of C=O and C=C, respectively, which demonstrate the existence of alkane, ketone, or carboxylic acids.

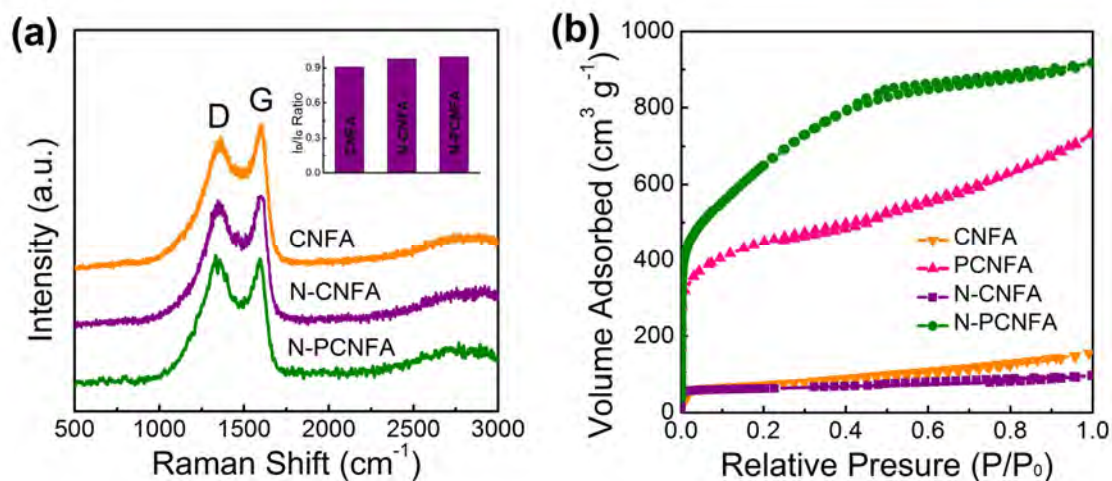


Fig. 4. (a) Raman spectroscopy of CNFA, N-CNFA, and N-PCNFA. (b) Nitrogen adsorption-desorption isotherm for CNFA, PCNFA, N-CNFA, and N-PCNFA.

The Raman spectra of CNFA, N-CNFA, and N-PCNFA are presented in Fig. 4a. The D-band is attributed to the amorphous carbon or defective graphitic structure, and the G-band is a characteristic feature of graphitic carbon. The intensity of I_D/I_G illustrates the disorder degree in the carbon structure [31, 32]. Compared with the I_D/I_G of CNFA (0.91) and N-CNFA (0.98), more defects can be generated through the N-doping. The I_D/I_G ratio of N-PCNFA (1.01) was higher than of N-CNFA, indicating that the KOH activation process could generate more defects on the carbon framework. The defects can increase the energy storage sites for LIBs and SCs to enhance the electrochemical performance. The N_2 adsorption/desorption analysis was used to measure the specific surface area and pore size distributions of N-PCNFA, N-CNFA, PCNFA, and CNFA. The N_2 adsorption/desorption isotherms show that the major absorption of the four samples presents at low relative pressure ($P/P_0 < 0.02$), which is corresponding to typical type I adsorption isotherm, confirming the adsorption in micropores (Fig. 4b). In addition, the isotherm of N-PCNFA also exhibits a hysteresis loop (typical type IV), arising from the mesoporous structure. The surface areas of N-PCNFA, N-CNFA, PCNFA, and CNFA are 2290, 1536, 199, and 242 $m^2 g^{-1}$, respectively, indicating the prominent surface areas of N-PCNFA and PCNFA result from the KOH activation treatment [33]. The pore size distributions of N-PCNFA and PCNFA calculated from the adsorption branch are mainly centered at between 1.5-4 nm, suggesting the formation of micropores and partly small-sized mesopores through N-doping and KOH activation (Fig. S3). The high surface area and micro-mesoporous structure can storage the electrolyte and increase the active material/electrolyte interface area

to promote the transport of ions, thus facilitating the rate performance for LIBs and SCs.

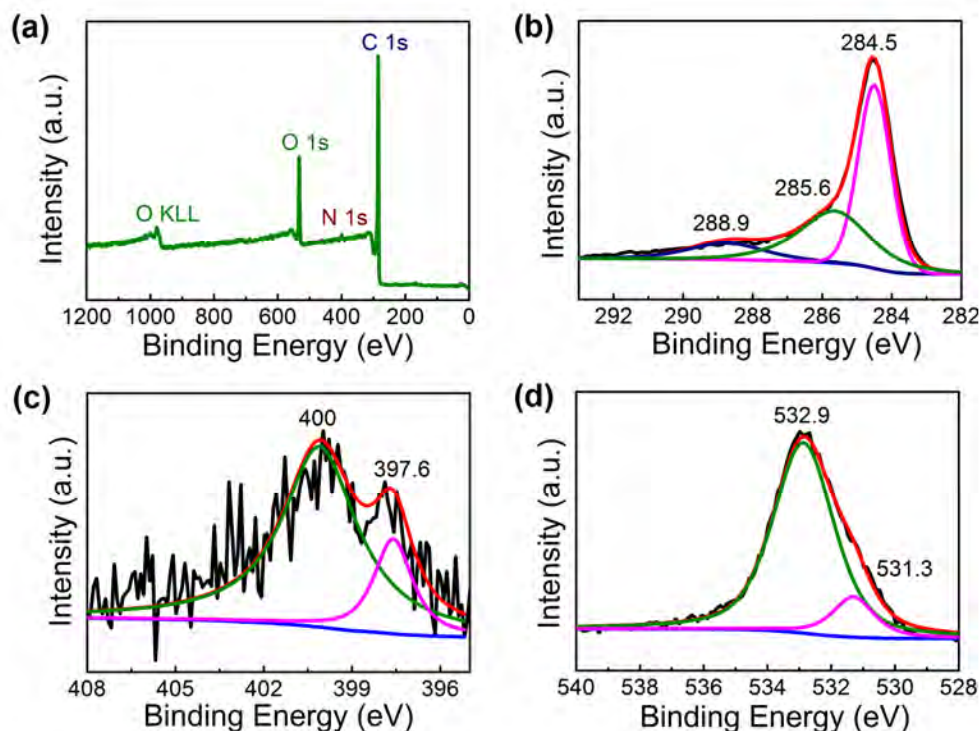


Fig. 5. XPS spectra of N-PCNFA, (a) full survey scan spectrum, (b) C 1s, (c) N 1s, and (d) O 1s spectra.

X-ray photoelectron spectroscopy (XPS) was used to identify the chemical state of element in N-PCNFA. The full survey spectrum shows three peaks located at about 284, 400, and 533 eV, corresponding to the characteristic peaks of C 1s, N 1s, and O 1s, respectively (Fig. 5a). XPS spectrum of N 1s was deconvoluted into two peaks positioned at 397.6 eV (pyridinic-N) and 400 eV (pyrrolic-N) (Fig. 5b) [34, 35]. Such N-containing structure in the carbon framework can enhance the electrochemical conductivity of the sample, favouring the binding of electrolyte ions [36]. Fig. 5c shows the C 1s spectrum of the N-PCNFA. Three peaks located at 284.5, 285.6, and 288.9 eV correspond to C=C and C-C, C-O, and O-C=O,

respectively. Furthermore, the deconvoluted spectrum for O 1s with two peaks located at 531.3 and 532.9 eV are assigned to C = O and C-OH groups, respectively (Fig. 5d). The C 1s and O 1s spectra indicate the residual oxygen-containing groups bonded with C atom in N-PCNFA after the pyrolysis and activation process [37].

3.2 The electrochemical properties

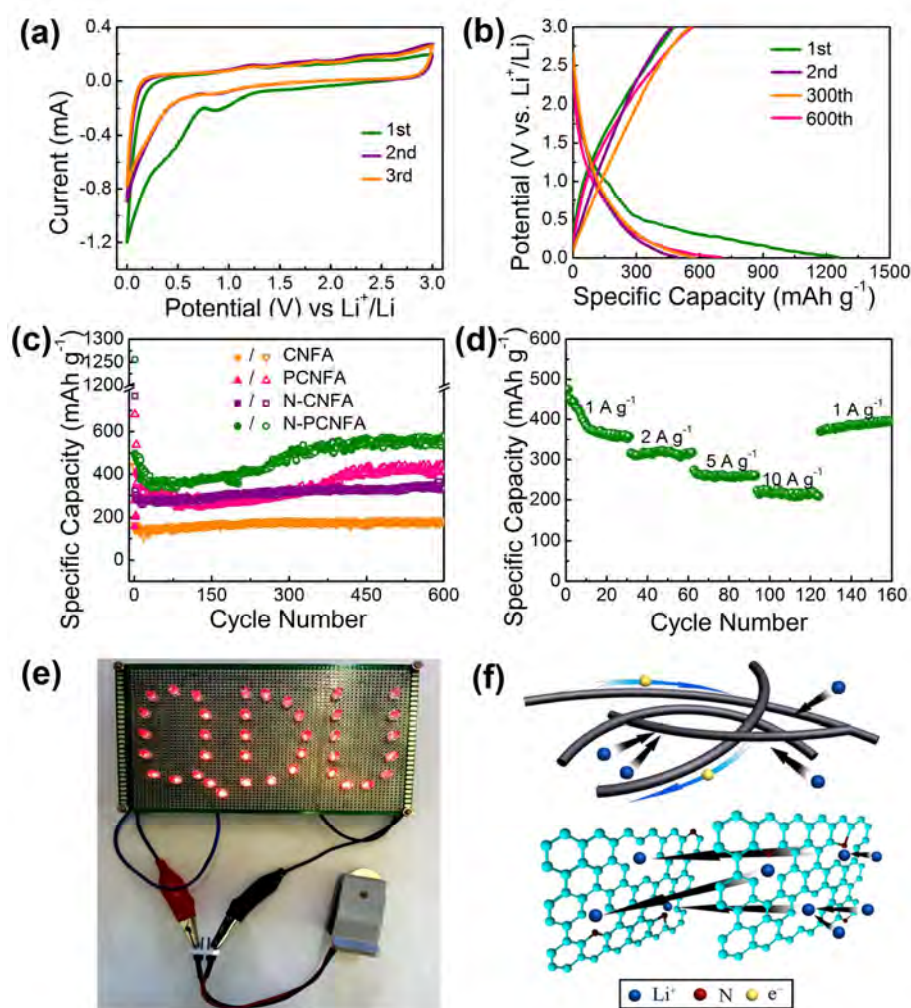


Fig. 6. (a) CV curves of N-PCNFA at different cycles. (b) The galvanostatic charge/discharge curves of N-PCNFA cycled at the 1st, 2nd, 300th, and 600th between 0.01 and 3.0 V (vs. Li^+/Li) at a current density of 1 A g^{-1} . (c) Specific capacity comparisons at different cycles of CNFA, PCNFA, N-CNFA, and N-PCNFA at a current

density of 1 A g^{-1} . (d) The charge specific capacity of the N-PCNFA at different current densities. (e) The optical image of the LEDs lit by one half-cell using N-PCNFA and Li metal foil as electrodes. (f) Schematic illustration of the advantages of N-PCNFA in enhancing lithium storage performance.

The electrochemical properties of the samples as lithium storage materials were examined in a half-cell test by cyclic voltammetry (CV) and galvanostatic cycling techniques. Fig. 6a exhibits the CV curves of N-PCNFA electrode, which show the typical curves of carbon-based materials. For the first cycle, the reduction peaks at 0.53 and 0.87 V in the cathodic scan are attributed to the formation of solid electrolyte interphase (SEI) layer. Both peaks disappear from the second cycle because that the passivation SEI layer prevents the decomposition of electrolyte. The integrated area intensity in the third cycle is nearly unchanged compared with the second one, suggesting the good cycling stability of the N-PCNFA electrode. The GCD curves of the N-PCNFA at 1 A g^{-1} (vs. Li^+/Li , 0.01-3.0 V) are shown in Fig. 6b. For the first discharge curve, the discharge plateaus at around 0.9 and 0.5 V was due to the formation of SEI layer, corresponding to the CV curve of the first cycle. The first charge and discharge specific capacities of N-PCNFA are 480 and 1256 mAh g^{-1} with a low coulombic efficiency of 38.2 %. The specific capacity becomes stable after the first cycle. The N-PCNFA exhibits high charge specific capacity and excellent stability (572 mAh g^{-1} at current densities of 1 A g^{-1} over 600 cycles). Under the identical conditions, the CNFA, PCNFA, and N-CNFA present a charge specific capacity of 182, 422, and 347 mAh g^{-1} after 600 cycles, respectively (Fig. 6c). The increased capacity of N-PCNFA and PCNFA after cycling should be ascribed to the continuous activation process of the highly porous carbon [35]. The rate performance of N-PCNFA was evaluated at the

current densities of 1, 2, 5, and 10 A g⁻¹ for 30 cycles (Fig. 6d). The N-PCNFA can be reversibly charged to 320, 263 and 220 mAh g⁻¹ at the current densities of 2, 5, and 10 A g⁻¹, respectively. When the current density returned back to 1 A g⁻¹ after 120 cycles, the specific capacity can be increased to 380 mAh g⁻¹. As shown in Fig. 6e, the light-emitting diodes (LEDs) were lit by one CR2016-type coin cell using N-PCNFA and Li metal foil as electrodes, implying the N-PCNFA is a high performance lithium storage material.

The unique N-doped hierarchical porous nanofibrous of N-PCNFA showed high capacity, excellent stability and rate performance as lithium storage material. As illustrated in Fig. 6f, the 3D structured CNF aerogel with interconnected hierarchical pores can provide channels for electron transport, which is crucial for promoting the conductivity of the electrode. The N-doping and activation processes can generate more defects in the carbon frameworks, allowing more Li⁺ diffuse into inner carbon to explore more lithium storage sites, and the N-doping can improve electrochemical conductivity to enhance the electron transport, which has been proved by the electrochemical impedance spectroscopy (Fig. S4) [38, 39]. Furthermore, The N atoms doped in the carbon framework are favourable to bind with Li⁺ to enhance the specific capacity and rate performance of the sample [40].

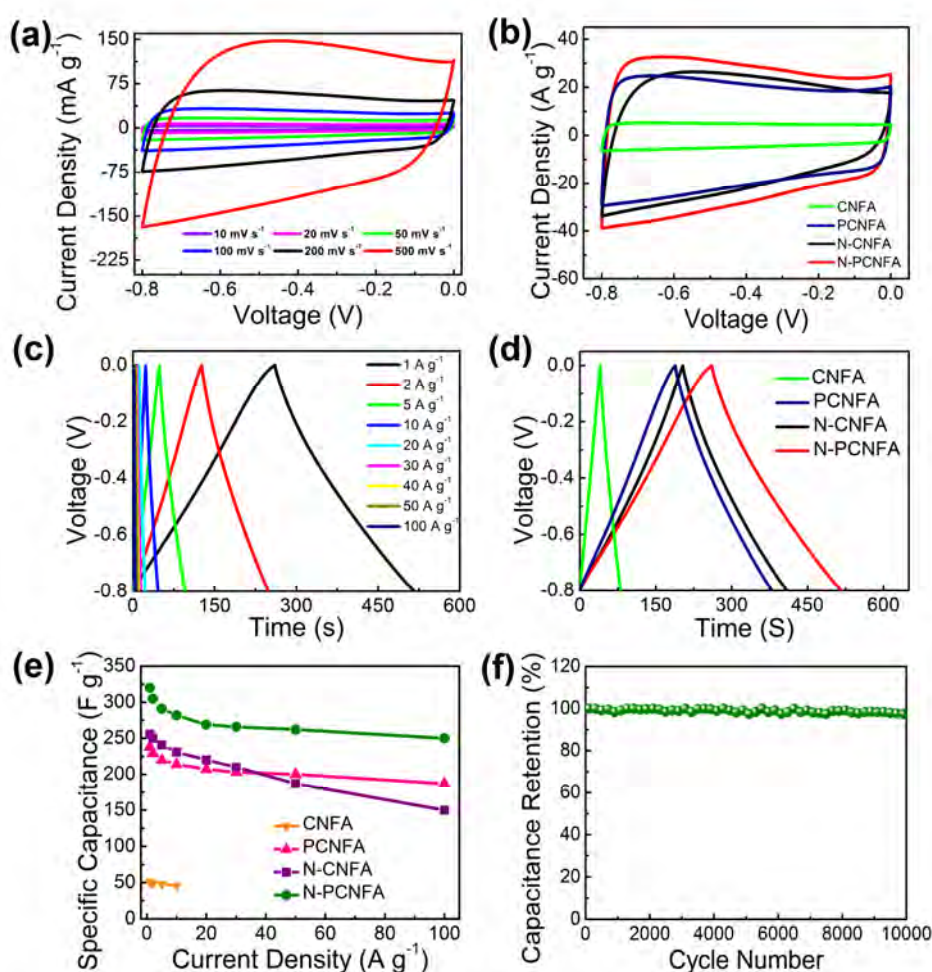


Fig. 7. Electrochemical performance characteristics measured in a three-electrode system. (a) CV curves of N-PCNFA in 6.0 M KOH solution between -0.8 and 0 V at different scan rates. (b) CV curves of CNFA, PCNFA, N-CNFA, and N-PCNFA in 6.0 M KOH solution at a scan rate of 100 mV s⁻¹. (c) Galvanostatic charge/discharge curves of N-PCNFA at different current densities. (d) Galvanostatic charge/discharge curves of CNFA, PCNFA, N-CNFA, and N-PCNFA at the current density of 1 A g⁻¹. (e) The specific capacitances of CNFA, PCNFA, N-CNFA, and N-PCNFA at various current densities. (f) Capacitance retention ratio for N-PCNFA at a current density of 5 A g⁻¹ for 10000 cycles.

The electrochemical performances of samples for SCs were tested using three-electrode system (6 M KOH as electrolyte). Especially, we tested the samples directly without addition of binder. Fig. 7a shows the CV curves of the N-PCNFA at different scan rates. All of the CV curves display a typical rectangular shape between -0.8 and 0 V. The CV curves of N-CNFA, PCNFA, and CNFA also exhibit rectangular shape (Fig. 7b and S5). Fig. 7c presents the GCD curves of N-PCNFA at different current densities with the symmetric curves, indicating the excellent electric double layer capacitive properties. The specific capacitances of N-PCNFA are determined to be 320, 291, 282, 269, 262, and 248 F g⁻¹ at the current densities of 1, 5, 10, 20, 50, and 100 A g⁻¹, respectively. The specific capacitance of N-PCNFA at high current density of 100 A g⁻¹ can still keep about 78.4 % of that value at 1 A g⁻¹, highlighting the excellent rate performance of N-PCNFA. Comparing the GCD curves of CNFA, PCNFA, N-CNFA, and N-PCNFA at current density of 1 A g⁻¹ (Fig. 7d and S6), the discharge time of the N-PCNFA is longer than that of others, indicating the N-PCNFA offers a higher specific capacitance. The rate performances of CNFA, PCNFA, N-CNFA, and N-PCNFA are also shown in Fig. 7e. The N-PCNFA has the highest specific capacitances at all the current densities among the samples, illustrating that the N-doping and KOH activation processes can intensely enhance the electrochemical performance for SCs. Moreover, the PCNFA exhibits better rate performance than that of N-CNFA. In addition, the N-PCNFA suffers from the issue of low volumetric capacitance attributed to the highly porous structure and low density [41], nevertheless, the N-CNFA with low surface area may show higher volumetric capacitance than those of N-PCNFA and PCNFA. The cycling

stability of N-PCNFA is also excellent and the specific capacitance remains 92.4 % after 10000 cycles at 10 A g^{-1} (Fig. 7f).

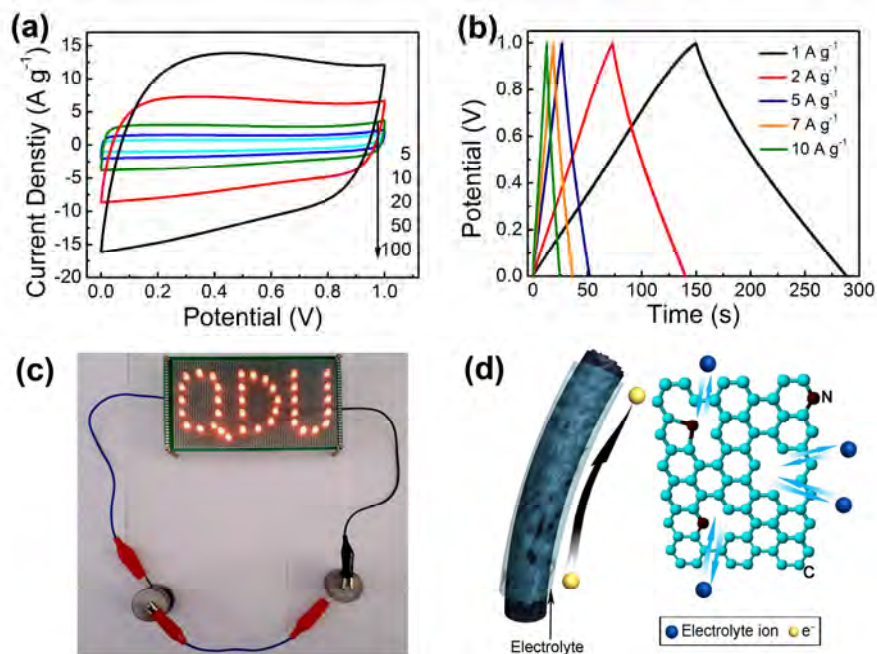


Fig. 8. Electrochemical performance characteristics measured in a two-electrode system. (a) CV curves of N-PCNFA in 6.0 M KOH solution between 0 and 1 V at different scan rates. (b) Galvanostatic charge/discharge curves of N-PCNFA at different current densities. (c) The optical image of the LEDs lit by two SCs in series using N-PCNFA as electrodes. (d) Schematic illustration of the advantages of N-PCNFA in enhancing SCs.

We also fabricated a symmetric capacitor with the N-PCNFA as electrodes to evaluate the electrochemical performance in practical SCs application. The CV curves of N-PCNFA in a two-electrode system also display rectangular shape between 0 and 1.0 V (Fig. 8a), suggesting in the excellent double-layer capacitive performance. Fig. 8b shows the GCD curves of the two-electrode system with symmetric shape and the specific capacitances are 278, 268, 251, 246, and 239 F g^{-1} at 1, 2, 5, 7, and 10 A g^{-1} .

Table 1 summaries the electrochemical performances of carbon materials for supercapacitors, which the N-PCNFA electrode exhibits high capacitance performance. However, the amorphous structured N-PCNFA shows inferior capacitance performance compared the heteroatoms-doped graphene aerogels [42, 43]. The two symmetric SCs using N-PCNFA-based electrodes in series can also light the LEDs (Fig. 8c). As the electrode material for SCs, the specific capacitance and rate performance of N-PCNFA is higher than that of N-free and pore-less samples. As shown in Fig. 8d, the N-doping not only improves electronic conductivity of the sample, but also enhances the charge density of the carbon framework to promote the adsorption of electrolyte ions and generate pseudocapacity [16]. In addition, the large surface area and micro-mesoporous structure increase the interface between electrolyte and active sites and shorten the diffusion distance of electrolyte ions, thus enhancing the double layer capacitance and rate performance.

Table 1. Comparison of the electrochemical performances of carbon aerogels based two-electrode supercapacitor.

| Carbon material | BET specific surface area | Specific capacitance (F g ⁻¹) | Electrolyte | Reference |
|---|---------------------------|---|------------------------------------|-----------|
| Hierarchical porous carbon aerogel | 2200 | 255 (1.0 A g ⁻¹) | 6 M KOH | [5] |
| Three-dimensional, S-incorporated graphene aerogel | 359.5 | 445.6 (5.0 mV S ⁻¹) | 1 M H ₂ SO ₄ | [42] |
| P-incorporated graphenes with hierarchical architecture | 383 | 353 (1.0 A g ⁻¹) | 1 M H ₂ SO ₄ | [43] |
| N-doped porous carbon/graphene aerogel | 473 | 290 (1.0 A g ⁻¹) | 1 M H ₂ SO ₄ | [44] |
| N-doped graphene aerogel | 830 | 223 (0.2 A g ⁻¹) | 1 M H ₂ SO ₄ | [45] |
| B/N co-doped porous carbon network | 2666 | 214 (0.2 A g ⁻¹) | 6 M KOH | [46] |
| Hierarchical carbon foam | 2772 | 240 (1.0 A g ⁻¹) | 1 M H ₂ SO ₄ | [47] |
| Graphene-carbon nanotube foam architecture | 743 | 286 (1.78 mA cm ⁻²) | 6 M KOH | [48] |
| Graphene oxide sponges | 239.2 | 247.6 (1.0 A g ⁻¹) | 1 M H ₂ SO ₄ | [49] |
| Hierarchical porous graphene frameworks | 829 | 278.5 (5.0 mV S ⁻¹) | 1 M H ₂ SO ₄ | [50] |
| N-PCNFA | 2290 | 278 (1.0 A g ⁻¹) | 6 M KOH | This work |

4. Conclusions

We successfully explored the N-doped porous carbon nanofiber aerogel using the residue of *gelidium amansii* after extraction of agar as precursor with a large surface area and micro-mesoporous structure as high-performance multifunctional energy storage material. The unique structure of 1 D, N-doping, and porous structure plays a crucial part in promoting the energy storage performance of the carbon-based materials. Given the utilization of the residue of agar production, this work opens a new way in increasing utilization rate of earth-abundant seaweed resource for developing low-cost and large-scale nanostructured carbonaceous energy storage materials *via* a green pathway and promotes the development of seaweed industry and energy storage material industry.

Acknowledgements

We are grateful for the financial support by the National Natural Science Foundation of China (grant no. 51473081 and 51672143), Taishan Scholars Program, and Outstanding Youth of Natural Science in Shandong Province (JQ201713), and ARC Discovery Project (No. 170103317).

Appendix A. Supplementary data

Supplementary data related to this article can be found at <https://doi>.

References

- [1] F. Béguin, V. Presser, A. Balducci, E. Frackowiak, Carbons and electrolytes for advanced supercapacitors, *Adv. Mater.* 26 (2014) 2219-2251.
- [2] L.-F. Chen, X.-D. Zhang, H.-W. Liang, M. Kong, Q.-F. Guan, P. Chen, Z.-Y. Wu, S.-H. Yu, Synthesis of nitrogen-doped porous carbon nanofibers as an efficient electrode material for supercapacitors, *ACS Nano* 2 (2012) 7092-7102.
- [3] Y. Chen, X. Li, K. Park, J. Song, J. Hong, L. Zhou, Y.W. Mai, H. Huang, J.B. Goodenough, Hollow carbon-nanotube/carbon-nanofiber hybrid anodes for Li-ion batteries, *J. Am. Chem. Soc.* 135 (2013) 16280-16283.
- [4] Y. Chen, X. Li, X. Zhou, H. Yao, H. Huang, Y.-W. Mai, L. Zhou, Hollow-tunneled graphitic carbon nanofibers through Ni-diffusion-induced graphitization as high-performance anode materials, *Energy Environ. Sci.* 7 (2014) 2689-2696.
- [5] J. Cui, Y. Xi, S. Chen, D. Li, X. She, J. Sun, W. Han, D. Yang, S. Guo, Prolifera-green-tide as sustainable source for carbonaceous aerogels with hierarchical pore to achieve multiple energy storage, *Adv. Funct. Mater.* 26 (2016) 8487-8495.
- [6] L. Dai, D.W. Chang, J.B. Baek, W. Lu, Carbon nanomaterials for advanced energy conversion and storage, *Small* 8 (2012) 1130-1166.
- [7] M.S. Dresselhaus, A. Jorio, M. Hofmann, G. Dresselhaus, R. Saito, Perspectives on carbon nanotubes and graphene Raman spectroscopy, *Nano Lett.* 10 (2010) 751-758.
- [8] J.L. Goldfarb, G. Dou, M. Salari, M.W. Grinstaff, Biomass-based fuels and activated carbon electrode materials: an integrated approach to green energy systems, *ACS Sustainable Chem. Eng.* 5 (2017) 3046-3054.
- [9] K. Gupta, T. Liu, R. Kaviani, H.G. Chae, G.H. Ryu, Z. Lee, S.W. Leeb, S. Kumar, High surface area carbon from polyacrylonitrile for high-performance electrochemical capacitive energy storage, *J. Mater. Chem. A* 4 (2016) 18294-18299.
- [10] Z. Hu, L. Wang, K. Zhang, J. Wang, F. Cheng, Z. Tao, J. Chen, MoS₂ nanoflowers with expanded interlayers as high-performance anodes for sodium-ion batteries, *Angew. Chem. Int. Ed.* 53 (2014) 12794-12798.

- [11] C. Kim, K.S. Yang, M. Kojima, K. Yoshida, Y.J. Kim, Y.A. Kim, M. Endo, Fabrication of electrospinning-derived carbon nanofiber webs for the anode material of lithium-ion secondary batteries, *Adv. Funct. Mater.* 16 (2006) 2393-2397.
- [12] A.A. Koós, F. Dillon, R.J. Nicholls, L. Bulusheva, N. Grobert, N-SWCNTs production by aerosol-assisted CVD method, *Chem. Phys. Lett.* 538 (2012) 108-111.
- [13] M. Kruk, M. Jaroniec, Gas adsorption characterization of ordered organic-inorganic nanocomposite materials, *Chem. Mater.* 13 (2001) 3169-3183.
- [14] B. Li, F. Dai, Q. Xiao, L. Yang, J. Shen, C. Zhang, M. Cai, Activated carbon from biomass transfer for high-energy density lithium-ion supercapacitors, *Adv. Energy Mater.* 6 (2016) 1600802.
- [15] B. Li, F. Dai, Q. Xiao, L. Yang, J. Shen, C. Zhang, M. Cai, Nitrogen-doped activated carbon for a high energy hybrid supercapacitor, *Energy Environ. Sci.* 9 (2016) 102-106.
- [16] D. Li, C. Lv, L. Liu, Y. Xia, X. She, S. Guo, D. Yang, Egg-box structure in cobalt alginate: a new approach to multifunctional hierarchical mesoporous N-doped carbon nanofibers for efficient catalysis and energy storage, *ACS Cent. Sci.* 1 (2015) 261-269.
- [17] D. Li, D. Yang, X. Yang, Y. Wang, Z. Guo, Y. Xia, S. Sun, S. Guo, Double-helix structure in carrageenan-metal hydrogels: a general approach to porous metal sulfides/carbon aerogels with excellent sodium-ion storage, *Angew. Chem. Int. Ed.* 55 (2016) 15925-15928.
- [18] D. Li, D. Yang, X. Zhu, D. Jing, Y. Xia, Q. Ji, R. Cai, H. Li, Y. Che, Simple pyrolysis of cobalt alginate fibres into $\text{Co}_3\text{O}_4/\text{C}$ nano/microstructures for a high-performance lithium ion battery anode, *J. Mater. Chem. A* 2 (2014) 18761-18766.
- [19] Y. Li, Z.-Y. Fu, B.-L. Su, Hierarchically structured porous materials for energy conversion and storage, *Adv. Funct. Mater.* 22 (2012) 4634-4667.
- [20] L. Liu, X. Yang, C. Lv, A. Zhu, X. Zhu, S. Guo, C. Chen, D. Yang, Seaweed-derived route to Fe_2O_3 hollow nanoparticles/N-doped graphene aerogels with

- high lithium ion storage performance, *ACS Appl. Mater. Interfaces* 8 (2016) 7047-7053.
- [21] L. Liu, X. Yang, N. Ma, H. Liu, Y. Xia, C. Chen, D. Yang, X. Yao, Scalable and cost-effective synthesis of highly efficient Fe₂N-based oxygen reduction catalyst derived from seaweed biomass, *Small* 12 (2016) 1295-1301.
- [22] Y. Lu, Q. Sun, X. She, Y. Xia, Y. Liu, J. Li, D. Yang, Fabrication and characterisation of alpha-chitin nanofibers and highly transparent chitin films by pulsed ultrasonication, *Carbohydr. Polym.* 98 (2013) 1497-1504.
- [23] Y. Lu, G. Ye, X. She, S. Wang, D. Yang, Y. Yin, Sustainable Route for Molecularly Thin Cellulose Nanoribbons and Derived Nitrogen-Doped Carbon Electrocatalysts, *ACS Sustainable Chem. Eng.* 5 (2017) 8729-8737.
- [24] N. Ma, Y.A. Jia, X. Yang, X. She, L. Zhang, Z. Peng, X. Yao, D. Yang, Seaweed biomass derived (Ni,Co)/CNT nanoaerogels: efficient bifunctional electrocatalysts for oxygen evolution and reduction reactions, *J. Mater. Chem. A* 4 (2016) 6376-6384.
- [25] Q. Ma, Y. Yu, M. Sindoro, A.G. Fane, R. Wang, H. Zhang, Carbon-based functional materials derived from waste for water remediation and energy storage, *Adv. Mater.* 29 (2017) 1605361.
- [26] J.H. Park, J.Y. Hong, H.C. Jang, S.G. Oh, S.H. Kim, J.J. Yoon, Y.J. Kim, Use of *Gelidium amansii* as a promising resource for bioethanol: a practical approach for continuous dilute-acid hydrolysis and fermentation, *Bioresour. Technol.* 108 (2012) 83-88.
- [27] Y.B. Seo, Y.W. Lee, C.H. Lee, H.C. You, Red algae and their use in papermaking, *Bioresour. Technol.* 101 (2010) 2549-2553.
- [28] J. Sun, C. Lv, F. Lv, S. Chen, D. Li, Z. Guo, W. Han, D. Yang, S. Guo, Tuning the shell number of multishelled metal oxide hollow fibers for optimized lithium-ion storage, *ACS Nano* 11 (2017) 6186-6193.
- [29] T. Tamura, H. Kawakami, Aligned electrospun nanofiber composite membranes for fuel cell electrolytes, *Nano Lett.* 10 (2010) 1324-1328.
- [30] Z. Tan, K. Ni, G. Chen, W. Zeng, Z. Tao, M. Ikram, Q. Zhang, H. Wang, L. Sun, X. Zhu, X. Wu, H. Ji, R.S. Ruoff, Y. Zhu, Incorporating pyrrolic and

- pyridinic nitrogen into a porous carbon made from C60 molecules to obtain superior energy storage, *Adv. Mater.* 29 (2017) 1603414.
- [31] D. Weingarth, M. Zeiger, N. Jäckel, M. Aslan, G. Feng, V. Presser, Graphitization as a universal tool to tailor the potential-dependent capacitance of carbon supercapacitors, *Adv. Energy Mater.* 4 (2014) 1400316.
- [32] K.N. Wood, R. O'Hayre, S. Pylypenko, Recent progress on nitrogen/carbon structures designed for use in energy and sustainability applications, *Energy Environ. Sci.* 7 (2014) 1212-1249.
- [33] Z.-S. Wu, W. Ren, L. Xu, F. Li, H.-M. Cheng, Doped graphene sheets as anode materials with superhigh rate and large capacity for lithium ion batteries *ACS Nano* 5 (2011) 5463-5471.
- [34] J. Xu, F. Xu, M. Qian, F. Xu, Z. Hong, F. Huang, Conductive carbon nitride for excellent energy storage, *Adv. Mater.* 29 (2017) 1701674.
- [35] G. Ye, X. Zhu, S. Chen, D. Li, Y. Yin, Y. Lu, S. Komarnenid, D. Yang, Nanoscale engineering of nitrogen-doped carbon nanofiber aerogels for enhanced lithium ion storage, *J. Mater. Chem. A* 5 (2017) 8247-8254.
- [36] S.B. Yoon, G.S. Chai, S.K. Kang, J.-S. Yu, K.P. Gierszal, M. Jaroniec, Graphitized pitch-based carbons with ordered nanopores synthesized by using colloidal crystals as templates, *J. Am. Chem. Soc.* 127 (2005) 4188-4189.
- [37] M. Yu, Y. Zhang, Y. Zeng, M.S. Balogun, K. Mai, Z. Zhang, X. Lu, Y. Tong, Water surface assisted synthesis of large-scale carbon nanotube film for high-performance and stretchable supercapacitors, *Adv. Mater.* 26 (2014) 4724-4729.
- [38] B. Zhang, F. Kang, J.-M. Tarascon, J.-K. Kim, Recent advances in electrospun carbon nanofibers and their application in electrochemical energy storage, *Prog. Mater. Sci.* 76 (2016) 319-380.
- [39] W. Zhao, P. Yuan, X. She, Y. Xia, S. Komarneni, K. Xi, Y. Che, X. Yao, D. Yang, Sustainable seaweed-based one-dimensional (1D) nanofibers as high-performance electrocatalysts for fuel cells, *J. Mater. Chem. A* 3 (2015) 14188-14194.

- [40] Y. Zou, S. Chen, X. Yang, N. Ma, Y. Xia, D. Yang, S. Guo, Suppressing Fe-Li antisite defects in LiFePO₄/carbon hybrid microtube to enhance the lithium ion storage, *Adv. Energy Mater.* 6 (2016) 1601549.
- [41] J.Y. Hong, J.J. Wie, Y. Xu, H.S. Park, Chemical modification of graphene aerogels for electrochemical capacitor applications, *Phys. Chem. Chem. Phys.* 17 (2015) 30946-30962.
- [42] X. Yu, S.K. Park, S.H. Yeon, H.S. Park, Three-dimensional, sulfur-incorporated graphene aerogels for the enhanced performances of pseudocapacitive electrodes, *J. Power Sources* 278 (2017) 484-489.
- [43] X. Yu, H.J. Kim, J.Y. Hong, Y.M. Jung, K.D. Kwon, J. Kong, H.S. Park, Elucidating surface redox charge storage of phosphorus-incorporated graphenes with hierarchical architectures, *Nano Energy* 15 (2015) 576-586.
- [44] C. Wang, Y. Huang, H. Pan, J. Jiang, X. Yang, Z. Xu, H. Tian, S. Han, D. Wu, Nitrogen-Doped Porous Carbon/Graphene Aerogel with Much Enhanced Capacitive Behaviors, *Electrochim. Acta* (215) 2016 100-107.
- [45] Z.Y. Sui, Y.N. Meng, P.W. Xiao, Z.Q. Zhao, Z.X. Wei, B.H. Han, Nitrogen-Doped Graphene Aerogels as Efficient Supercapacitor Electrodes and Gas Adsorbents, *ACS Appl. Mater. Interfaces* (7) 2015 1431-1438.
- [46] B. You, F. Kang, P.Q. Yin, Q. Zhang, Hydrogel-derived heteroatom-doped porous carbon networks for supercapacitor and electrocatalytic oxygen reduction, *Carbon* (103) 2016 9-15.
- [47] M. Oschatz, L. Borchardt, K. Pinkert, S. Thieme, M. R. Lohe, C. Hoffmann, M. Benusch, F. M. Wisser, C. Ziegler, Hierarchical Carbide-Derived Carbon Foams with Advanced Mesostructure as a Versatile Electrochemical Energy-Storage Material, *Adv. Energy Mater.* (4) 2014 1300645.
- [48] W. Wang, S. Guo, M. Penchev, I. Ruiz, K. N. Bozhilov, D. Yan, M. Ozkan, C. S. Ozkan, Three dimensional few layer graphene and carbon nanotube foam architectures for high fidelity supercapacitors, *Nano Energy* (2) 2013 294-303.
- [49] J.Y. Hong, X. Yu, B.M. Bak, C. Pang, H.S. Park, Bio-inspired functionalization and redox charge transfer of graphene oxide sponges for pseudocapacitive electrodes, *Carbon* (83) 2015 71-78.

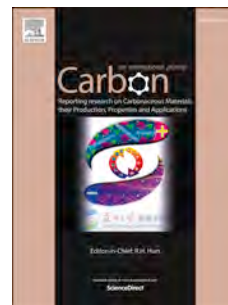
- [50] S. Yun, S.O. Kang, S. Park, H.S. Park, CO₂-activated, hierarchical trimodal porous graphene frameworks for ultrahigh and ultrafast capacitive behavior, *Nanoscale* (6) 2014 5296-5302.

ACCEPTED MANUSCRIPT

Accepted Manuscript

Turning *gelidium amansii* residue into nitrogen-doped carbon nanofiber aerogel for enhanced multiple energy storage

Daohao Li, Yu Wang, Yuanyuan Sun, Yun Lu, Shuai Chen, Bingbing Wang, Huawei Zhang, Yanzhi Xia, Dongjiang Yang



PII: S0008-6223(18)30471-8

DOI: [10.1016/j.carbon.2018.05.011](https://doi.org/10.1016/j.carbon.2018.05.011)

Reference: CARBON 13137

To appear in: *Carbon*

Received Date: 9 February 2018

Revised Date: 8 April 2018

Accepted Date: 4 May 2018

Please cite this article as: D. Li, Y. Wang, Y. Sun, Y. Lu, S. Chen, B. Wang, H. Zhang, Y. Xia, D. Yang, Turning *gelidium amansii* residue into nitrogen-doped carbon nanofiber aerogel for enhanced multiple energy storage, *Carbon* (2018), doi: 10.1016/j.carbon.2018.05.011.

This is a PDF file of an unedited manuscript that has been accepted for publication. As a service to our customers we are providing this early version of the manuscript. The manuscript will undergo copyediting, typesetting, and review of the resulting proof before it is published in its final form. Please note that during the production process errors may be discovered which could affect the content, and all legal disclaimers that apply to the journal pertain.